Experiments in Fluids (2025) 66:201
https://doi.org/10.1007/s00348-025-04131-9

RESEARCH ARTICLE

Mach–Zehnder interferometry for transient shock-dominated flows in a confined duct

Takahiro Yamashita[1] · Masaki Okajima[1] · Hiroki Kodama[1] · Shinichiro Nakao[1] · Yoshiaki Miyazato[1]

Received: 28 June 2025 / Revised: 3 October 2025 / Accepted: 6 October 2025

Abstract

Effective quantitative visualization of compressible flows across the full field of view is essential for understanding the flow topology and dynamics of supersonic jet oscillations, shock-boundary-layer interactions, and shock reflection and diffraction. The present study provides a methodology for obtaining the time-dependent density field of transient shock-dominated flows within a confined duct. A shock strong enough to induce flow separation and exhibiting unsteady behavior is introduced downstream of the throat within a divergent half duct. The incoming flow Mach number just upstream of the shock is approximately 1.47, and the Reynolds number calculated based on the height and flow properties at the throat is 1.35×10^5. We employ Mach-Zehnder interferometry with a finite-fringe setup to capture the time-resolved density field including the shock motion, utilizing a He-Ne laser as the light source and a high-speed camera as the recording device. A two-dimensional Fourier fringe analysis is employed to extract the phase information over the entire density field. Fascinating visual representations, such as the pseudo-infinite interferogram and the density field with phase information known as domain coloring, are introduced to illustrate flow topology. The oscillatory characteristics of shock motions are analyzed using both Lagrangian and Eulerian approaches, and the results are compared quantitatively. Furthermore, an uncertainty analysis is conducted to assess the accuracy of the density measurements and to reveal how shock oscillations affect density uncertainty.

1 Introduction

When supersonic flows in a Laval nozzle, inlet diffuser, or centrifugal compressor are decelerated to subsonic speeds, shock waves are typically generated (Matsuo et al. 1999). It is well-known that when a shock wave occurs in a confined duct, it interacts with the boundary layer that develops along the wall (Matsuo et al. 1999). This interaction results in a complex shock structure that may include a Mach stem and oblique shocks, or it can lead to a shock train composed of multiple shocks. These phenomena significantly contribute to the noise produced by the exhaust. Currently, various hypotheses have been proposed to explain the causes of shock oscillations including turbulence upstream of the shock, vortices that are periodically emitted from separation bubbles beneath the foot of the shock, and resonance effects related to the length of the flow path downstream of the shock. However, many unknowns still exist regarding the mechanisms that drive shock oscillations.

In recent years, various numerical studies of unsteady flows involving shock waves have been conducted using both commercial software, such as ANSYS Fluent, and open-source numerical codes like SU2. However, these studies always require verification with experimental results, and yet there are still few reliable experimental data with high spatial resolution over a full range of an interaction between a shock wave and the wall boundary layers in a confined channel. Thus, the validation of simulation results still requires experimental verification and accurate prior information,

Masaki Okajima, Hiroki Kodama, Shinichiro Nakao, Yoshiaki Miyazato have contributed equally to this work.

✉ Yoshiaki Miyazato
miyazato@kitakyu-u.ac.jp

Takahiro Yamashita
yamalab193@gmail.com

Masaki Okajima
masaki486921ryuutai@gmail.com

Hiroki Kodama
kodama_hsgd@outlook.com

Shinichiro Nakao
s-nakao@kitakyu-u.ac.jp

[1] Department of Mechanical Systems Engineering, The University of Kitakyushu, 1-1 Hibikino, Wakamatsu-ku, Kitakyushu, Fukuoka 808-0135, Japan

Published online: 18 October 2025

highlighting the ongoing relevance of improving optical measurement techniques.

Quantifying regions dominated by shock waves presents significant experimental challenges, particularly in unsteady flow fields. Intrusive probes such as Pitot tubes and hotwire anemometers, while commonly used for measuring physical quantities in supersonic jets, introduce several complications. In supersonic flows, a bow shock inevitably forms ahead of the probe, causing the measured pressure to deviate from the true total pressure and resulting in a reduction in the recorded value (Rathakrishnan 2019). Additionally, the presence of shock waves and rapid transitions from supersonic to subsonic flow can lead to substantial measurement errors. To minimize blockage effects, the ratio of the jet's cross-sectional area to the projected area of the Pitot probe must exceed 64 (Rathakrishnan 2019). Furthermore, the insertion of probes disturbs the flow field, altering the jet characteristics and compromising measurement fidelity. A critical limitation of conventional Pitot tubes is their inherently low temporal resolution, which renders them unsuitable for capturing dynamic shock oscillations. As a result, pressure-based diagnostic techniques to obtain unsteady shock characteristics have relied on two approaches: (1) embedding flush-mounted pressure sensors at the wall surface near the shock foot (Dolling et al. 1985; Dolling and Smith 1989), and (2) employing a movable static pressure port along the duct centerline, known as a movable throughtube, to enhance temporal resolution (Matsuo et al. 1993). While both methods have demonstrated effectiveness in detecting shock-induced oscillatory phenomena, they are fundamentally limited to pointwise measurements and cannot resolve the spatially distributed and temporally evolving nature of shock wave dynamics.

In contrast, standard shadowgraphy and schlieren methods (Settles 2001) are effective visualization techniques for studying supersonic flows and are frequently employed for the validation of numerical simulations. However, these methods predominantly emphasize the qualitative aspects of the flow. On the other hand, the application of optical diagnostic techniques utilizing tracer particles, such as Laser Doppler Anemometry (LDA), Particle Image Velocimetry (PIV), and Laser-Induced Fluorescence (LIF), to measure physical quantities within supersonic jets presents several significant challenges (Feng and McGuirk 2016; Yoo et al. 2010; Yüceil 2017). Firstly, ensuring that tracer particles accurately and promptly follow the flow dynamics is particularly difficult in regions where the flow transitions rapidly from supersonic to subsonic before and after a strong shock wave. Secondly, discrepancies between the dimensions and density of the tracer particles and the fluid can lead to erroneous measurements, as the particles may not perfectly mimic the fluid's motion. To overcome the limitations of PIV, which suffers from the so-called velocity slip error immediately after a shock wave due to its reliance on tracking solid or liquid particles, research has been conducted on molecular tagging velocimetry (MTV) (Lempert et al. 2002), which tracks molecules instead. Sakurai et al. (2015) developed an MTV system using acetone as a tracer molecule and quantitatively compared the velocity distributions obtained by MTV and PIV around the Mach disk in an underexpanded jet. Their results demonstrated that the velocity distribution obtained by PIV scarcely captured the sharp velocity drop caused by the shock wave, in contrast to the MTV measurements. Furthermore, the development of MTV systems using krypton as a tracer molecule suggests promising future advancements in this technique (Parziale et al. 2015).

Laser interferometry with infinite-fringe settings can visualize the flow while capturing the density field simultaneously. Szumowski et al. (1995) elucidated the shock behavior exhibiting three representative oscillation patterns within the Laval nozzle using the Mach-Zehnder interferometry with the infinite-fringe setting. However, this technique has the drawback of poor spatial resolution and requires prior knowledge of whether the density in the flow field is increasing or decreasing to obtain accurate density measurements. On the other hand, laser interferometry using finite-fringe settings can produce high-resolution density fields. Still, it is challenging to determine the magnitude of phase shifts relative to the background fringes. Consequently, there is active development of measurement techniques to investigate regions dominated by shock waves without the use of tracer particles. It is noteworthy that Settles' seminal work on flow visualization introduces a practical method for generating interference fringes by integrating a Wollaston prism into a schlieren optical system—a technique known as Wollaston Prism Shearing Interferometry (WPSI) (Settles 2001). While WPSI provides access to the density gradient field rather than the density field itself, it is highly effective for visualizing flow fields with strong density gradients, such as shock waves, and has been applied to the visualization of shock structures around spiked blunt bodies in supersonic flows (Srulijes et al. 2000).

Recently, quantitative visualization methods have been developed to analyze the time-averaged structure of shock waves in external flows. These methods include background-oriented schlieren (Ota et al. 2011; Settles and Hargather 2017), rainbow schlieren deflectometry (Takeshita et al. 2023), and Mach-Zehnder interferometry (Takeshita et al. 2019; Telega et al. 2022). Takeshita et al. (2019) employed finite-fringe Mach-Zehnder interferometry to obtain time-resolved measurements of the density field associated with a shock train in a constant-area straight duct. However, due to the alignment of the reference fringe wavefronts perpendicular to the flow direction, accurate detection of fringe shifts near the shock waves was limited. A close inspection of the

recorded interferograms reveals noticeable distortions in the fringe patterns near the shock waves. While such distortions may, in general, be attributed to steep optical density gradients, it is also prudent to consider that, under low-density and high Mach number conditions, chemical and vibrational relaxation processes could contribute to fringe deformation. In the case of Takeshita et al. (2019), however, the Mach number is relatively low (approximately 1.5), and thus the influence of such relaxation effects is expected to be negligibly small. Telega et al. (2022) successfully measured a stationary normal shock in a two-dimensional Laval nozzle using Mach-Zehnder interferometry with a finite-fringe setting. By configuring the optical system to align the reference interference fringe wavefronts perpendicular to the flow direction, they achieved precise acquisition of the density field near the shock waves. However, they did not investigate the unsteady characteristics of the shock waves.

In recent developments, Focused Laser Differential Interferometry (FLDI) (Parziale et al. 2013; Settles and Fulghum 2016; Marsh et al. 2024) has emerged as a highly effective optical diagnostic technique for capturing small-scale density fluctuations in high-speed flow environments. In a comprehensive review, Benitez et al. (2025) present recent advancements in FLDI theory, instrumentation, and practical applications, encompassing multi-point measurement configurations, computational modeling approaches, and integration with complementary diagnostic methods. Particular emphasis is placed on FLDI's utility in investigating hypersonic boundary-layer transition, characterizing freestream turbulence, and analyzing reacting flows. In parallel, Quadrature Fringe Imaging Interferometry (QFII) (Wang et al. 2022) is gaining attention as a promising technique for high-precision measurement of steep refractive index gradients, particularly those occurring across shock fronts.

In this study, we propose a method for measuring transient shock-dominated flows in a confined duct using Mach-Zehnder interferometry with the finite-fringe setting. A two-dimensional Fourier transform method is employed to analyze fringe shifts in the interference fringes, irrespective of the orientation of the reference fringe wavefronts. In addition, we demonstrate intriguing visualization representations, including pseudo-infinite-fringe interferograms, bright-field schlieren, and density fields with phase information. Furthermore, the oscillatory characteristics of a shock motion are demonstrated using the Lagrangian and Eulerian approaches. Finally, an uncertainty analysis is performed on the density field obtained using the current Mach-Zehnder system.

2 Experimental methods

2.1 Experimental facility

Experiments were carried out in an intermittent blowdown compressible air facility with a Mach-Zehnder interferometer. The air supplied by a compressor that pressurizes the ambient air to 2.0 MPa is filtered, dried, and stored in a reservoir with a total capacity of 4 m^3. The high-pressure dry air from the reservoir enters a plenum chamber through a coupling, as shown in Fig. 1, and is then stagnated and exhausted to the atmosphere through a test section. In the present experiment, the plenum pressure (p_{os}) is controlled and maintained constant during testing by a solenoid valve.

As shown in Fig. 2, a test section is a two-dimensional half duct with straight bottom and divergent upper walls. The duct has heights of 18.0 mm, 6.0 mm, and 12.0 mm at the inlet, throat, and exit, respectively, which is a constant

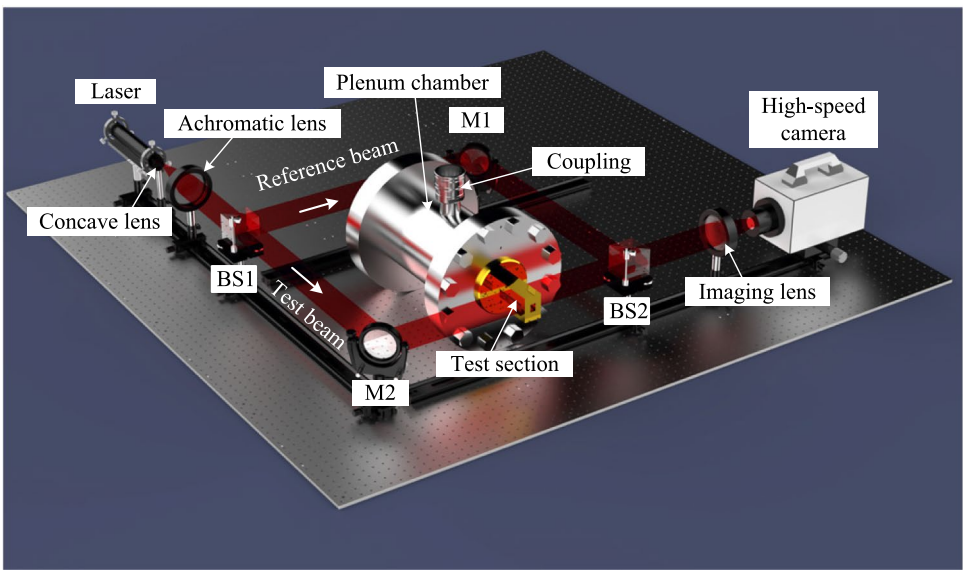

Fig. 1 Schematic drawing of the experimental apparatus with Mach-Zehnder interferometer. A He-Ne laser with a wavelength of 632.8 nm is used as the light source. BS1 and BS2 denote beamsplitters, M1 and M2 plane mirrors. High-pressure dry air is supplied to the plenum chamber through the coupling

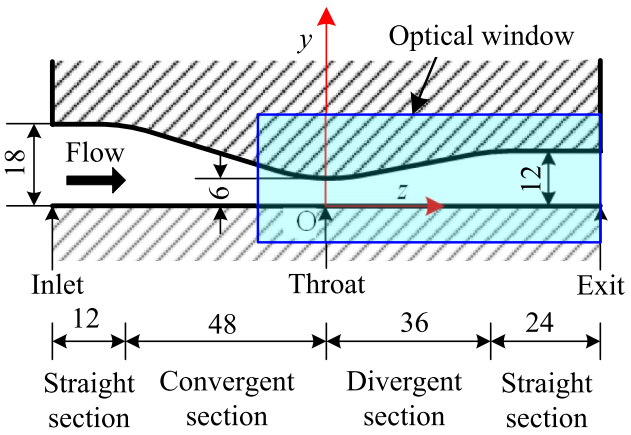

Fig. 2 Schematic drawing of the test section with the dimensions in millimeters. The test section has a constant spanwise width of 15 mm from the inlet to the exit and a design Mach number of 2.20

spanwise width of 15 mm over the full length from the inlet to the exit. The design Mach number derived from the exit-to-throat area ratio is 2.2. The test section was manufactured from a brass block using a cut-processing machine (Kitamura Machinery, Mycenter-3XG) with a positioning accuracy of $\pm 2\mu$m and a repeatability of $\pm 1\mu$m. The area surrounded by the solid blue line represents an optical window, and the flow field in a part of this area is measured by Mach-Zehnder interferometry.

Experiments are performed at an operating pressure ratio of $p_{os}/p_b = 1.5$ within an accuracy of 1.0 % to produce a shock wave downstream of the throat. The back pressure p_b is 101.8 kPa $\pm$ 0.5 kPa and the room temperature T_b is 298.3 K within an accuracy of about 0.1 K during the experiments. The Reynolds number based on the height and flow properties at the throat is $Re_{th} = 1.35 \times 10^5$. Experiments are repeated at least five times for the same operating pressure ratio to obtain statistics such as time average, standard deviation, precision error, etc.

2.2 Optical instrumentation

Mach-Zehnder interferometry based on the finite-fringe setting is used to visualize quantitatively time-resolved density fields with an oscillating shock in a confined duct. A Helium-Neon (He-Ne) laser (Sigma Koki, model 05-LHP-925), characterized by a wavelength of 632.8 nm, an output power of 5 mW, and a beam diameter of 0.48 mm, is employed as the light source. As shown in Fig. 1, after passing through a convex lens, the beam is collimated by an achromatic lens with a diameter of 100 mm and a focal length of 500 mm before reaching the first beamsplitter (BS1), which divides it into reference and test beams. The reference beam is reflected by the plane mirror (M1), directed to the second beamsplitter (BS2), traversing a quiescent atmosphere with uniform density. Meanwhile, the test beam is reflected by plane mirror (M2) and passes through the test section to the second beamsplitter (BS2), where the two beams overlap again.

The propagation direction for the reference and test beams just before entering the camera can be altered by rotating M1 and M2 around a vertical axis or a horizontal plane, respectively. In the present experiment, the fringe spacing and direction of the interferograms on the camera's recording device are controlled by adjusting the angle of M1, which alters the propagation direction of the reference beam. Interferograms of the flows through the test section are recorded in 5,000 pictures with 24,000 frames per second and an exposure time of 3.21 μs via a high-speed camera (Photoron, Fastcam SA1.1).

3 Fringe shift analysis

3.1 Interaction between reference and test beams

When the test beam passes through a test section with a variable refractive index field, the background fringes are changed into deformed fringe patterns. As shown in Fig. 3a, for simplicity, we first consider the reference and test beams after the beams pass through the BS2 (see Fig. 1) as plane waves. The coordinate x is the direction of the optical axis, in which the test beam propagates after being reflected at Mirror 2 (M2) as shown in Fig. 1. The coordinates y and z form the vertical plane perpendicular to the x direction. The reference beam Ψ_r travels in the direction that forms angles α, β, and γ with respect to the x-, y-, and z- axes, respectively, and the test beam Ψ_t propagates in the positive direction of the x axis.

If the reference and test beams have the same phase φ_0 at $x = t = 0$ without being influenced by the refractive index fields, they can be expressed as follows:

$$\Psi_r(\mathbf{r}, t) = a \exp\left[i\left(\mathbf{k}_r \cdot \mathbf{r} - \omega t + \varphi_0\right)\right] \tag{1}$$

$$\Psi_t(\mathbf{r}, t) = a \exp\left[i\left(\mathbf{k}_t \cdot \mathbf{r} - \omega t + \varphi_0\right)\right] \tag{2}$$

where ω and a are an angular frequency and an amplitude of light in still air, and t is the time. In addition, $\mathbf{k}_r$ and $\mathbf{k}_t$ are the angular wave vectors, and $\mathbf{r}$ is the position vector, which are given by

$$\mathbf{k}_r = \frac{2\pi}{\lambda_a}(\cos\alpha, \cos\beta, \cos\gamma), \quad \mathbf{k}_t = \frac{2\pi}{\lambda_a}(1, 0, 0), \quad \mathbf{r} = (x, y, z) \tag{3}$$

Here, λ_a is the wavelength of light in still air.

As shown in Fig. 3a, if the test beam undergoes a path difference d in propagation distance through changes in refractive index, the resultant test wave Ψ_t' becomes

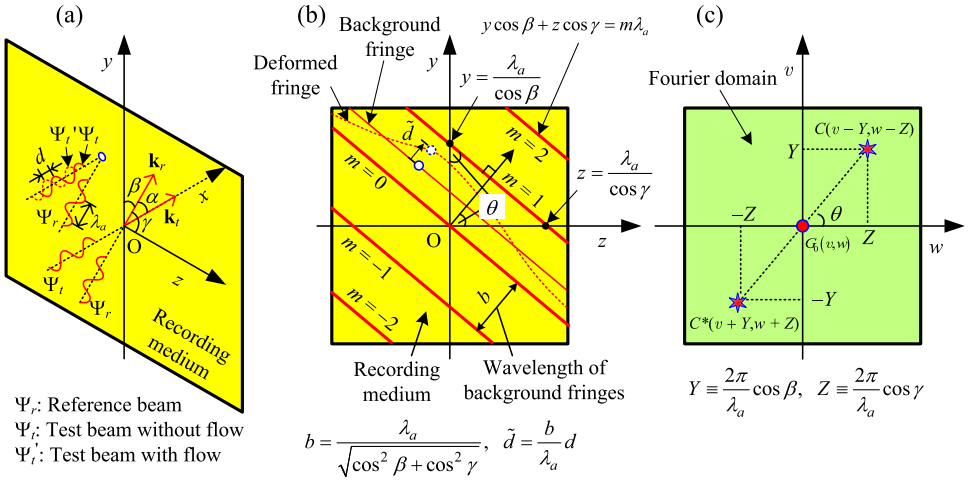

Fig. 3 Conceptual diagram illustrating the two-dimensional Fourier transform from spatial to Fourier domain for both background and deformed fringe patterns, showing (a) interaction between reference and test beams, (b) resulting fringe patterns on the detector plane at $x = 0$, and (c) their spectral representations in the Fourier domain, with coordinate system defined such that x denotes the optical axis direction, y the vertical direction, and z the flow direction

$$\Psi_t'(\mathbf{r},t) = a\exp\left[i\left(\mathbf{k}_t\cdot\mathbf{r} - \omega t + \varphi_0 - \frac{2\pi}{\lambda_a}d\right)\right] \tag{4}$$

If Ψ_r and Ψ_t are superimposed on a recording medium located at $x = 0$, resultant intensity field can be expressed as

$$g_r(y,z) = \left|\Psi_r(\mathbf{r},t) + \Psi_t(\mathbf{r},t)\right|^2 = 2a^2 + 2a^2\cos\left[\left(\mathbf{k}_t - \mathbf{k}_r\right)\cdot\mathbf{r}\right] \tag{5}$$

This intensity varies in a sinusoidal form. Therefore, there are local maxima at the following conditions.

$$\left(\mathbf{k}_t - \mathbf{k}_r\right)\cdot\mathbf{r} = 2\pi m \tag{6}$$

where m is an integer. Substitution of Eq. (3) into Eq. (6) leads to

$$y_m\cos\beta + z_m\cos\gamma = m\lambda_a \tag{7}$$

This implies that the intensity distribution has the maximum brightness on the straight line, as shown in Fig. 3b.

Using Eq. (7), the interval b between the background fringes on the medium ($x = 0$) is given by

$$b = \frac{\lambda_a}{\sqrt{\cos^2\beta + \cos^2\gamma}} \tag{8}$$

The interval b becomes narrower with increasing β and γ for $0 < \beta, \gamma < \pi/2$, and it shows infinite-fringe patterns for $\beta = \gamma = \pi/2$.

Similarly, from Eqs. (1) and (4), the intensity field experiencing changes in refractive index is given by

$$\begin{aligned} g_t(y,z) =& \left|\Psi_r(\mathbf{r},t) + \Psi_t'(\mathbf{r},t)\right|^2 \\ =& 2a^2 + 2a^2\cos\left[\left(\mathbf{k}_t - \mathbf{k}_r\right)\cdot\mathbf{r} - \frac{2\pi}{\lambda_a}d\right] \end{aligned} \tag{9}$$

The comparison of Eqs. (5) and (9) shows that g_t can be translated by a phase

$$\tilde{\varphi}(y,z) \equiv \frac{2\pi}{\lambda_a}d \tag{10}$$

or it can be converted into the corresponding path difference

$$\tilde{d} = \frac{b}{2\pi}\tilde{\varphi}(y,z) \tag{11}$$

Substitution of Eqs. (3) and (10) into Eq. (9) yields

$$g_t(y,z) = 2a^2 + 2a^2\cos\left[Yy + Zz - \tilde{\varphi}(y,z)\right] \tag{12}$$

on the recording medium ($x = 0$) where $Y = 2\pi\cos\beta/\lambda_a$ and $Z = 2\pi\cos\gamma/\lambda_a$.

3.2 Fourier transform method

Background and deformed fringe patterns taken with a digital camera are illustrated in Fig. 3b as the red solid and dotted lines, respectively, and denote lines of constant phase at $x = 0$ and $t = t_0$. The interval b in Fig. 3b represents the distance between two successive crests of the background fringes, and it is a function of the intersection angles (β and γ) between the reference and test beams and the wavelength (λ_a) of the laser light used in the experiment. When the recording medium is not $x = 0$ but at a fixed position and the reference and test beams have a different phase, the intensity profiles $g(y, z)$ for the background fringe and deformed fringe patterns can be given by

$$g_r(y,z) = g_0(y,z) + g_1(y,z)\cos\left[Yy + Zz + \Delta\right] \tag{13}$$

$$g_t(y,z) = g_0(y,z) + g_1(y,z)\cos\left[Yy + Zz + \Delta - \tilde{\varphi}(y,z)\right] \tag{14}$$

where Δ is the phase difference between the background fringe and deformed fringe patterns at the recording medium and it includes phase changes by optical imperfections of the instrument.

In this expression, $g_0(y,z)$ and $g_1(y,z)$ are used instead of a^2 in the first and second terms on the right-hand side of Eqs. (13) and (14), because the amplitude is modulated by a non-uniform light source, bias light, and noise (Telega et al. 2022).

The phase shift $\tilde{\varphi}(y,z)$ contains only the desired information on the density field. The intensity profile of the deformed fringe pattern expressed as Eq. (14) can be rewritten in the following expression:

$$g_t(y,z) = g_0(y,z) + c_t(y,z)\exp\left[i(Yy+Zz)\right] + c_t^*(x,y)\exp\left[-i(Yy+Zz)\right] \tag{15}$$

with

$$c_t(y,z) = \frac{g_1(y,z)}{2}\exp\left[i(\Delta-\tilde{\varphi}(y,z))\right] \tag{16}$$

where, i is the imaginary unit and the asterisk * denotes the complex conjugate.

The two-dimensional (2D) Fourier transform of Eq. (15) with respect to y and z is given by:

$$G_t(v,w) = G_0(v,w) + C_t(v-Y,w-Z) + C_t^*(v+Y,w+Z) \tag{17}$$

where the capital letters denote the 2D Fourier transforms of the respective primitive functions, e.g.,

$$G_t(v,w) = \int_{-\infty}^{\infty}\int_{-\infty}^{\infty} g_t(y,z)e^{-i(vy+wz)}dydz$$
$$g_t(y,z) = \frac{1}{4\pi^2}\int_{-\infty}^{\infty}\int_{-\infty}^{\infty} G_t(v,w)e^{i(vy+wz)}dvdw$$

with v and w being the spatial frequency coordinates. It should be noted that c_t^* is the complex conjugate of c_t, while C_t^* represents the 2D Fourier transform of c_t^*. If c_t is a complex variable, then the complex conjugate of the 2D Fourier transform C_t of c_t is not equal to C_t^*. If the complex conjugate of C_t is $\bar{C}_t$, then it can also be expressed as $C_t^*(v+Y,w+Z) = \bar{C}_t(-v-Y,-w-Z)$.

Since the spatial variations in $g_0(y,z)$, $g_1(y,z)$, and $\tilde{\varphi}(y,z)$ are slow compared with the spatial frequency Y and Z when the interval between fringes is sufficiently small, the Fourier spectra in Eq. (17) have three independent peaks, as schematically shown in Fig. 3c (Takeda 2013). We make use of either of these two spectra on the carrier, e.g., $C(v-Y,w-Z)$, and translate it by (Y,Z) on the wavenumber axis toward the origin to obtain $C(v,w)$ as shown in Fig. 3c for the case $\Delta = 0$ as a representative example.

Applying the inverse 2D Fourier transform of $C_t(v,w)$ with respect to v and w to obtain $c_t(y,z)$ and taking the logarithm of Eq. (16) leads to

$$\ln c_t(y,z) = \ln\frac{g_1(y,z)}{2} + i\left[\Delta-\tilde{\varphi}(y,z)\right] \tag{18}$$

Consequently, the phase shift $\tilde{\varphi}(y_0,z)$ in the imaginary part of Eq. (18) can be completely separated from the unwanted amplitude variation $g_1(y_0,z)$ in the real part.

$$\Delta-\tilde{\varphi}(y,z) = \mathrm{Im}\left[\ln c_t(y,z)\right] \tag{19}$$

A similar operation can be applied to the background fringes to obtain Δ. Finally, the phase shift $\tilde{\varphi}(y,z)$ can be obtained by the following relation:

$$\mathrm{Im}\left[\ln c_r(y,z)\right] - \mathrm{Im}\left[\ln c_t(y,z)\right] = \Delta - \left[\Delta-\tilde{\varphi}(y,z)\right] = \tilde{\varphi}(y,z) \tag{20}$$

To accurately estimate variations in optical path lengths for reconstructing density fields, it is essential to employ a phase-unwrapping procedure. This process is crucial for restoring continuous two-dimensional phase distributions. Phase map unwrapping involves converting the folded phase distribution back to its original continuous form, thereby eliminating any 2π jumps. In this study, we use a publicly available Python code implementing the phase-unwrapping algorithm proposed by Herráez et al. (2002), which has proven capable of reliably and accurately unwrapping phase data even in regions affected by measurement noise and large discontinuities such as the significant and discontinuous phase jumps across the shock front. Notably, Léon et al. (2022) have demonstrated that this algorithm can yield precise density fields even in areas with strong shock waves, such as Mach disks in underexpanded jets.

3.3 Reconstruction of density fields

The phase shift is related to variations in optical path lengths through the refractive indices $n(y,z)$ in the test section and n_a in the atmosphere, as follows (Merzkirch 2012):

$$\frac{\tilde{\varphi}(y,z)}{2\pi}\lambda_0 = \int_x^{x+L}\left[n(y,z)-n_a\right]dx \tag{21}$$

where $L = 15$ mm is the spanwise length of the test section, and λ_0 is the wavelength of a light source in a vacuum.

Carroll and Dutton (1990) investigated the interaction between a shock wave and turbulent boundary layers in a confined duct, under conditions where the freestream Mach number immediately upstream of the shock was 1.6, and the relative boundary-layer thickness was 0.40, normalized by the duct half-height. Their surface oil flow visualizations on both the upper and lower walls of the duct revealed that the flow structures within the shock-boundary-layer interaction region are predominantly two-dimensional, with the exception of small corner regions located beneath the foot of the first shock. Similarly, Atkin and Squire (1992)

examined shock wave/boundary-layer interactions over a range of incoming flow Mach numbers from 1.3 to 1.5. Their measurements of static pressure distributions along the tunnel span downstream of the shock indicated that the flow remains essentially two-dimensional across the central 88% of the tunnel width. In particular, for an incoming flow Mach number of 1.5, the flow maintains its uniform character across the span, with only minor deviations observed near the sidewalls. Accordingly, the analysis described below focuses on variations in the vertical (y) and streamwise (z) directions, under the premise that the flow field is spanwise uniform and the influence of sidewall boundary layers is minimal.

The density field in the test section is represented by

$$\rho(y,z) = \rho_a + \frac{\lambda_0}{2\pi KL}\tilde{\varphi}(y,z) \tag{22}$$

according to the Gladstone-Dale formula (Merzkirch 2012) given by $n(y,z) = 1 + K\rho(y,z)$ with the constant K ($= 2.2587 \times 10^{-4}$ m^3/kg).

To obtain a two-dimensional unsteady density field, it is necessary to know the reference density at a particular location at time $t = 0$. In the present experiments, the theoretical density value at the throat position is used as the reference density, because the flow from the plenum chamber to the throat can be assumed to be a steady isentropic flow. When the density at the throat position $(y/h^*, z/h^*) = (0.5,0)$ and time $t = 0$ is specified as ρ^* and the corresponding phase shift is $\tilde{\varphi}^*$, the two-dimensional unsteady density field at any time t can be expressed as

$$\frac{\rho(y,z,t)}{\rho_{os}} = \frac{\rho^*}{\rho_{os}} + \frac{\lambda_0}{2\pi KL\rho_{os}}\left[\tilde{\varphi}(y,z,t) - \tilde{\varphi}^*\right] \tag{23}$$

where the theoretical value of ρ^*/ρ_{os} is 0.6339 for a gas with a specific heat ratio of 1.4.

Since Eq. (23) shows that the phase shift at a fixed time is directly proportional to the flow density at the same time, characteristics of an unsteady flow field including an oscillating shock can be evaluated by examining the time history of the fringe shift. An image of the flow field in the test section by the Mach-Zehnder interferometer is formed onto the CMOS sensor of a high-speed camera (Photron, Fastcam SA1.1) which records a JPEG RGB image (8-bit each color) at a resolution of 1024 × 288 square pixels. The plane of focus is located in the front window of the test section. The RGB image is then turned into an 8-bit grayscale image by a linear transformation. Therefore, the distributions of background and deformed fringes with 256 different possible intensities can be calculated from the interferogram images for the density field in the test section.

Before reconstructing the density field using Eq. 23, Block-Matching and 3D (BM3D) filtering is employed to suppress noise. BM3D is a state-of-the-art denoising technique that groups similar image patches into a three-dimensional array and performs noise reduction via collaborative filtering in the transform domain. Renowned for its high accuracy and excellent preservation of fine structural details, BM3D has become a widely adopted method in natural image denoising. For a comprehensive description of the algorithm, refer to Mäkinen et al. (2020). In this study, Total Variation (TV) filtering was also applied for comparative purposes. However, the reconstructed density fields showed no significant differences between the BM3D and TV filtering approaches. The effective spatial resolution of the present Mach-Zehnder interferometer is approximately 31 μm/pixel in the object plane, which can be evaluated based on the physical and image dimensions of the test section. The time-resolved density fields are reconstructed from interferogram images using a custom-developed Python tool specifically designed and implemented in the authors' laboratory to support high-resolution optical diagnostics. This tool is intended to be made publicly accessible in the near future, following further refinement, validation, and documentation to ensure usability and reproducibility. A flowchart illustrating the entire process—from the acquisition of time-resolved finite-fringe images to the reconstruction of the corresponding density field—is provided in the Appendix for reference.

Note that when using images obtained by infinite-fringe Mach-Zehnder interferometry, the density fields can be evaluated (Smits and Lim 2012) by

$$\frac{\rho_i}{\rho_{os}} = \frac{\rho_r}{\rho_{os}} \pm \frac{\lambda_0}{KL\rho_{os}}(i-1) \tag{24}$$

in a nondimensional form where the integer i corresponds to the number of interference fringes measured relative to a known reference density, ρ_r. For the plus and minus signs, a minus sign is used when the density decreases from the reference density, and a plus sign is used when the density increases. Since isodensity lines appear in the interferograms of the flow field taken with the infinite-fringe setting, the densities of adjacent fringes are evaluated sequentially using Eq. (24) under the assumption that the densities on a single fringe are equal. However, as described below, isodensity lines have a certain width, which causes a large error in determining the density value.

The number of interference fringes is counted from the reference point to establish the density at each point in the flow field. The sign of the change in the phase shift is ambiguous, making it essential to understand the flow field when interpreting the results. However, the information needed to determine if the density is increasing or decreasing from the reference point is often derived from a basic understanding of fluid mechanics (Smits and Lim 2012).

It should be emphasized that the two-dimensional Fourier transform method employed in this study is theoretically formulated for a continuous and infinite spatial domain. In practice, however, the interferogram images are acquired over a discrete and finite domain, which inevitably introduces spectral artifacts into the spatial FFTs. These artifacts include spectral leakage due to abrupt truncation, sidelobes surrounding the principal frequency components, and potential aliasing effects. To mitigate these issues, appropriate windowing functions and careful spectral filtering techniques are essential. In the present study, we acknowledge the influence of rectangular windowing and have taken deliberate measures to isolate and extract the principal spectral components while minimizing the impact of these artifacts.

4 Results and discussion

4.1 Interferograms of shock-dominated flows

The finite-fringe interferograms without and with shock-dominated flows in a divergent half duct are shown in Fig. 4a and b, respectively. Figure 4a indicates parallel interference fringes set at $\theta = 45°$ to the lower wall surface. The spacing between two successive fringes is $b = 263$ μm. In Fig. 4b, the flow direction is from left to right. Comparing Fig. 4a and b, the interference fringes in the rectangular area surrounded by the blue dashed line are distorted due to the presence of a shock.

An example of interferograms taken by the Mach-Zehnder interferometry with an infinite-fringe setting is given in Fig. 5 with the flow direction from left to right. The experimental condition closely resembles that depicted in Fig. 4. Figure 5a and b displays the infinite-fringe interferograms taken without flow and with flow, respectively. These images experimentally capture the change in fringe patterns before and after the onset of flow, following the adjustment of the optical system to produce infinite fringes. Note that infinite-fringe patterns can be generated by gradually increasing the spacing between fringes in a finite-fringe interferogram, such as that shown in Fig. 4a, through optical system adjustment. Due to the slight shock oscillation around its time-averaged position, Fig. 5b represents a selection of several thousand images captured when the shock was nearly in the same location as shown in Fig. 4b. Comparing Figs. 4b, 5b shows a typical λ shock with large branches toward the upper wall, convex downstream in the central part, and smaller branches toward the lower wall, giving an obvious picture of the overall shape of the shock. The infinite-fringe interferogram can provide information on shock configurations. In addition, one can see how isopycnics change before and after the shock. Flow separation occurs from the foot of the leading shock of the upper branch

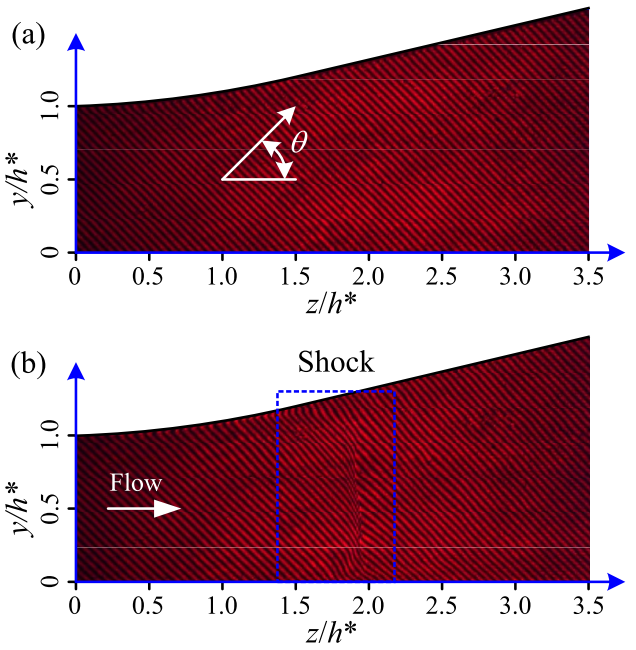

Fig. 4 Finite-fringe interferograms **a** without flow and **b** with flow including a shock. The background fringes are tilted at an angle of $\theta = 45°$ relative to the lower wall surface. The interval between two adjacent fringes is $b = 263$ μm. The shock exists in the rectangular area surrounded by the blue dashed line. The interferogram of (b) is taken with an exposure time of 1.0 μs. The incoming flow Mach number just upstream of the shock is approximately 1.47

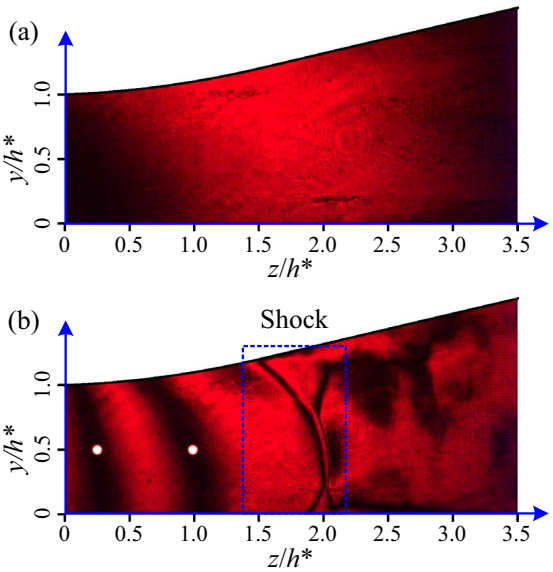

Fig. 5 Infinite-fringe interferograms **a** without flow and **b** with flow including a lambda shock. The lambda shock exists in the rectangular area surrounded by the blue dashed line. The interferogram of **b** is taken with an exposure time of 1.0 μs. The incoming flow Mach number just upstream of the shock is approximately 1.47. The density difference between the two white circles is $\Delta\rho/\rho_{os} = 0.105$ as a dimensionless value

shock. Given Eq. (24), the dimensionless density difference between two successive fringes is given by

$$\frac{\Delta\rho}{\rho_{os}} = \frac{\lambda_0}{KL\rho_{os}} = 0.105 \tag{25}$$

in the case of the present experiments. This value represents the difference in density between the two positions marked by the white circles in Fig. 5b.

The 2D Fourier transforms of the background and deformed fringe patterns, as shown in Fig. 4a and b, are presented in Fig. 6a and b, respectively. We can observe the spectra of the fringe patterns containing the phase modulation, respectively. The values of the spectra are highlighted using a logarithmic display. The correspondence between spectral magnitude and color is shown above the figure. The spectrum obtained from the two-dimensional Fourier transform of the fringe image is predominantly characterized by three distinct peaks: one located at the origin and two symmetrically positioned on either side. The central peak corresponds to the direct current (DC) component, representing the very low-frequency content and the spatially averaged intensity of the entire image (Telega et al. 2022). The two lateral peaks, referred to as the principal components, contain the primary fringe information. These components are distributed along a straight line inclined at an angle θ with respect to the w-axis. As depicted in Fig. 4a, this angle coincides with the direction normal to the wavefronts of the interference fringes. It is noteworthy that the spectral features indicated by red circles in Fig. 6a and b are artifacts introduced by the application of a rectangular window prior to the Fourier transformation of the finite-fringe interferograms shown in Fig. 4a and b. These artifacts arise due to the abrupt truncation of the image domain, which induces spectral leakage. The influence of the rectangular window further manifests as secondary features—commonly referred to as sidelobes—appearing as yellow streaks emerging from the DC and principal components in the spectral domain.

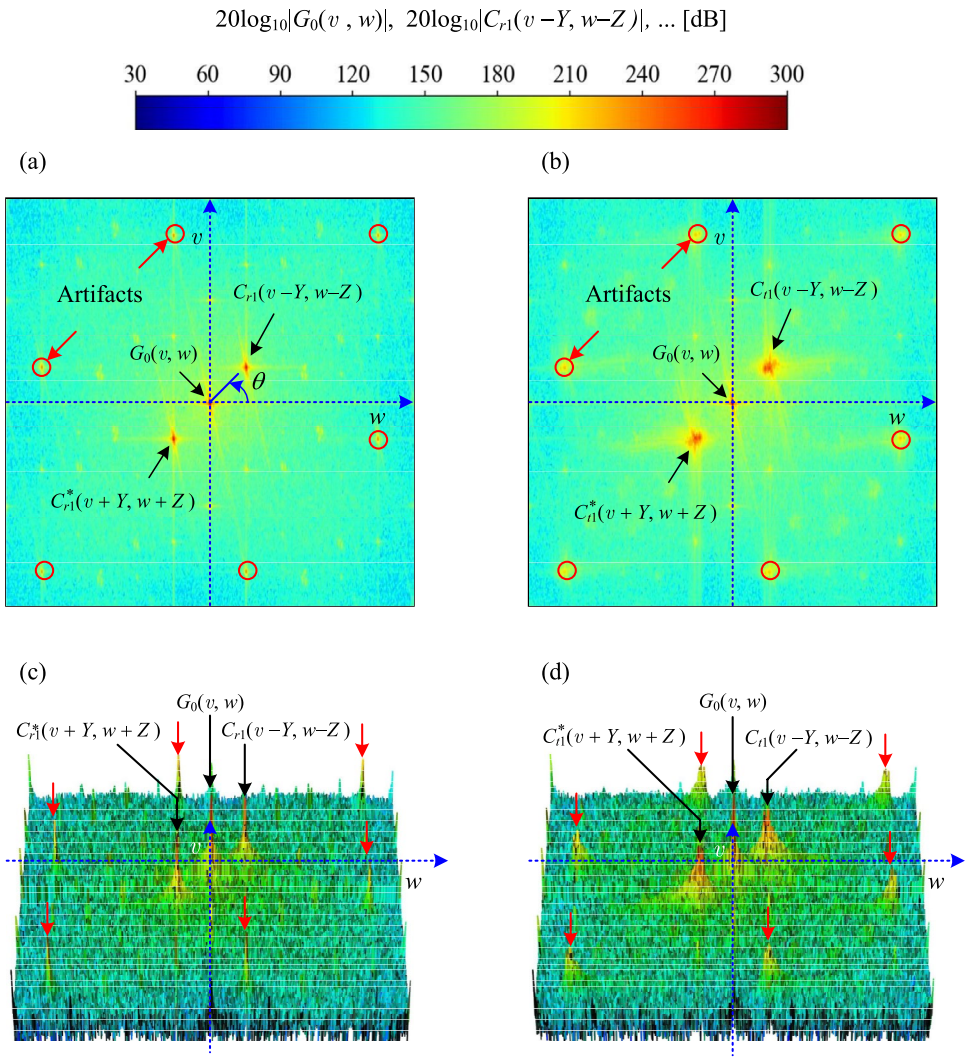

Fig. 6 Power spectra in modulus for the interferograms **a** without flow and **b** with flow, including the bird-eye views **c** and **d** corresponding to **a** and **b**, respectively. A logarithmic scale is used to represent the amplitude of the spectrum. The red circles in **a** and **b**, and the down-pointing arrows in **c** and **d** represent the spectra for artifacts

Comparison of Fig. 6a and b shows that fringe deformation changes the shape and magnitude of the peaks. Bird's-eye views of Fig. 6a and b are shown in Fig. 6c and d for reference where the down-pointing arrows represent the spectra for spurious fringes.

When comparing $C_{r1}(v-Y, w-Z)$ and $C_{t1}(v-Y, w-Z)$ in Fig. 6a and b, it can be seen that $C_{r1}(v-Y, w-Z)$ is concentrated almost as a point, while $C_{t1}(v-Y, w-Z)$ spans a wider area than $C_{r1}(v-Y, w-Z)$. In Fig. 4, the smaller the spacing (b) between two adjacent stripes of the background fringe, the more clearly $C_{t1}(v-Y, w-Z)$ and $C_{t1}(v+Y, w+Z)^*$ can be separated from $G_0(v, w)$ and the phase information can be extracted. In contrast, if the spacing between the strips is greater, a portion of $C_{t1}(v-Y, w-Z)$ and $C^*_{t1}(v+Y, w+Z)$ will overlap $G_0(v, w)$, making it impossible to obtain phase information $\tilde{\varphi}(y, z)$ (Winckler 1948; Sugawara et al. 2020). Note that when the stripe spacing is increased, infinite-fringe interferograms are produced.

4.2 Flow visualizations

Engaging visualizations can be developed based on Eq. (16). The pseudo-infinite-fringe interferograms of the shock-dominated flow in the divergent half duct are shown in Fig. 7a and b with the flow from left to right where these interferograms are 90° out of phase with each other. Black and white patterns indicate rough isodensity lines. From both figures, a two-dimensional shock structure bifurcating near the upper and lower wall surfaces can be clearly observed at $x/h^* =$ around 2.0. Furthermore, at the location of the throat ($x/h^* = 0$), the stripes are oblique rather than parallel to the y-axis because the curvature of the upper wall produces the vertical density gradient. In contrast, the finite-fringe interferogram in Fig. 4b does not reveal detailed flow and shock structures.

Figure 7c illustrates the visualization method known as domain coloring (Wegert 2012). This method effectively displays vector fields by showing both the magnitude and direction of the vectors simultaneously. The amplitude ($|c_t(y, z)|$) and phase ($arg\ c_t(y, z)$) of $c_t(y, z)$ are presented together. In other words, the information from Fig. 7a and b is comprehensively included in Fig. 7c. Notably, the phase $arg\ c_t(y, z)$ is given only modulo π since a rough visualization of the flow field is needed; precise phase information is unnecessary in this stage. Continuous phase connections are established when reconstructing the density field. In Fig. 7a and b, there are only two colors of isodensity lines—black and white. In contrast, Fig. 7c features multiple isodensity lines in various colors, such as red, blue, yellow, and green. This variety of colors enables a more detailed observation of the flow field.

Figure 8a presents the density field obtained from Fig. 4 through the analytical procedure detailed in Section 3. The density field is normalized to the stagnation density (ρ_{os})

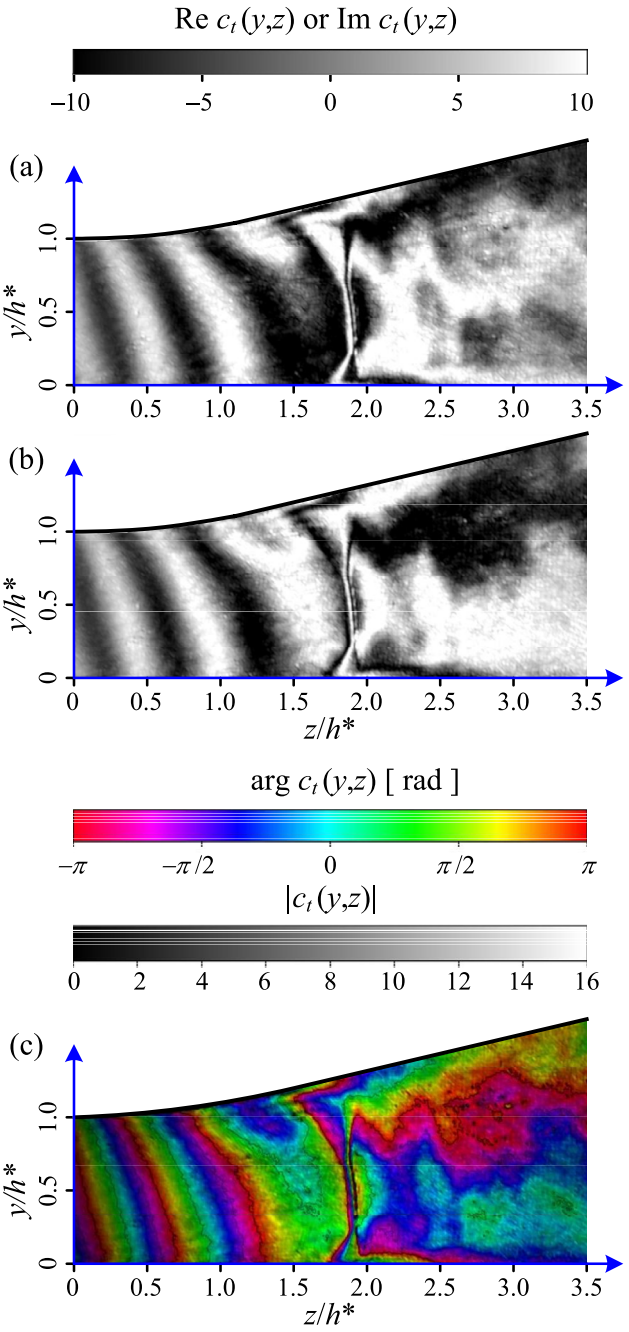

Fig. 7 Pseudo-infinite-fringe interferograms for **a** real part $Re\ c_t(y, z)$, **b** imaginary part $\Im\ c_t(y, z)$, and **c** domain coloring for $c_t(y, z)$

in the plenum chamber, located far upstream of the throat. The contour values correspond to the color scale displayed at the top of the figure. It should be noted that Fig. 8a is visually identical to Fig. 7, but it is presented quantitatively by density.

Figure 8b and c shows the density gradients in the z- and y-directions, respectively, derived from the density field in Fig. 8a. These correspond to vertical and horizontal schlieren images obtained using a conventional

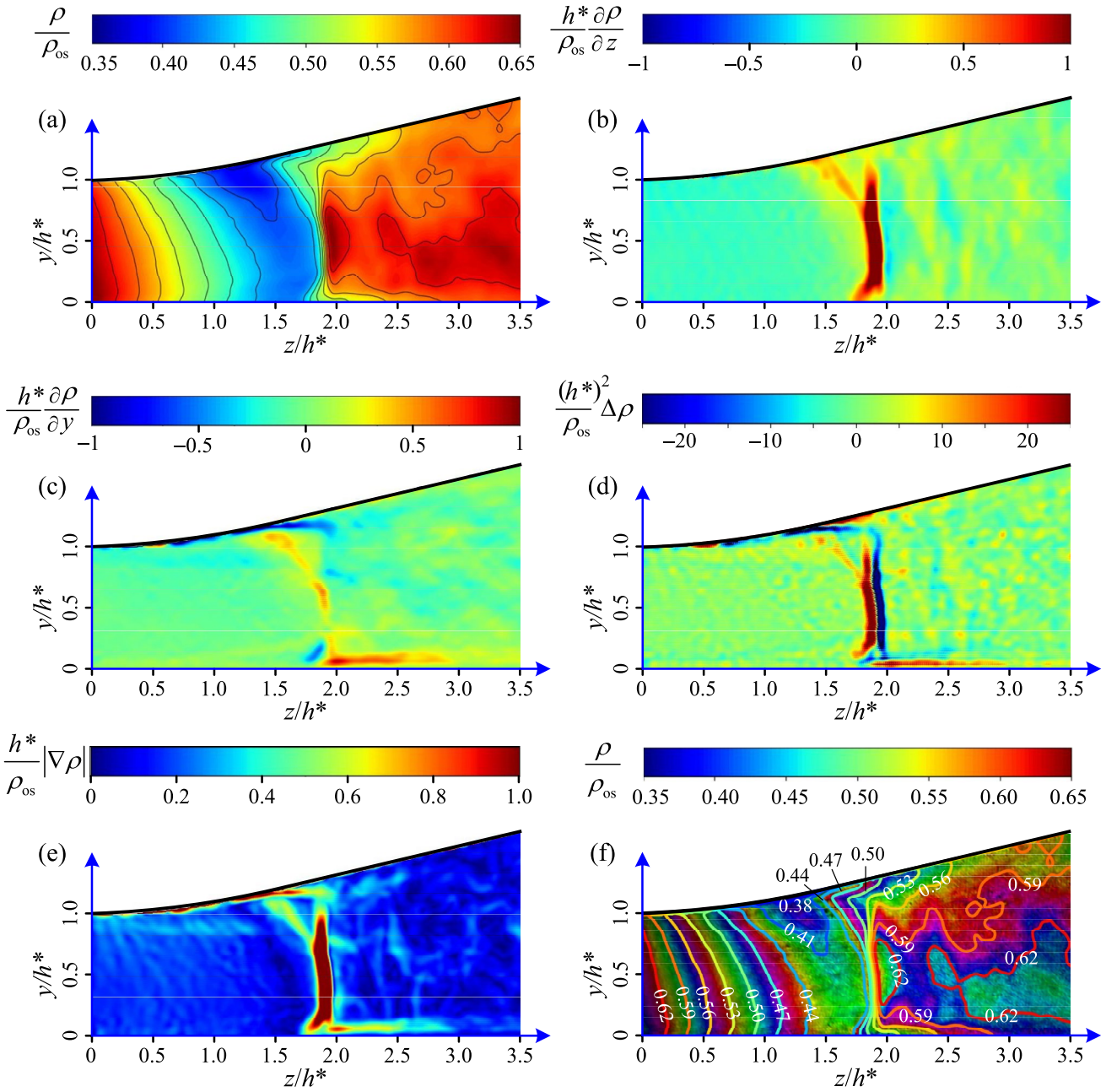

Fig. 8 Various flow visualizations corresponding to Fig. 4b with **a** density contour plots, **b** vertical cutoff schlieren, **c** horizontal cutoff schlieren, **d** shadowgraphy, and **e** bright-field schlieren, and **f** domain coloring with density contours

grayscale schlieren method with a knife edge. Figure 8d presents the nondimensional Laplacian of the density field, defined as the sum of its second-order partial derivatives in the z- and y-directions, expressed by the relation

$$\frac{(h^*)^2}{\rho_{os}}\Delta\rho = \frac{(h^*)^2}{\rho_{os}}\left(\frac{\partial^2\rho}{\partial y^2} + \frac{\partial^2\rho}{\partial z^2}\right) \tag{26}$$

This quantity corresponds to the shadowgraph image.

Figure 8b~(d) are all dimensionless, as indicated by the color bars above each figure. In shadowgraphy, shock waves always appear as dark lines accompanied by bright lines (Liepmann and Roshko 2001). In Fig 8d, the shock waves are represented by red lines corresponding to the bright lines and blue lines corresponding to the dark lines.

Shock structures and topology, including the spatial evolution of shock waves, shock-to-shock interactions,

and shock reflection and diffraction, can be quantitatively expressed through the magnitude of the density gradient vector given by

$$\frac{h^*}{\rho_{os}}|\nabla\rho| = \frac{h^*}{\rho_{os}}\sqrt{\left(\frac{\partial\rho}{\partial y}\right)^2 + \left(\frac{\partial\rho}{\partial z}\right)^2} \tag{27}$$

in nondimensional form (Sugawara et al. 2021). It indicates the degree of compression and expansion in every direction. This representation highlights the shock shapes and location of the onset of the expansion waves (Sugawara et al. 2021).

In general, the schlieren method displays the density gradient for a specific direction, such as perpendicular or parallel to the flow. However, Fig. 8e illustrates the magnitude of the density gradients in the radial direction, commonly referred to as the bright-field schlieren (Sugawara et al. 2021) or the circular cutoff schlieren (Settles and Hargather 2017). There are generally two methods for studying shock oscillations. The first method involves focusing on the time-averaged position of the oscillating shock and evaluating the density fluctuations at that position, which is known as Euler's method. The second method focuses on the motion of the shock itself to capture its oscillations, referred to as Lagrange's method. Bright-field schlieren imaging is particularly effective for studying shock oscillations using Lagrange's method. The shock oscillatory characteristics obtained from both methods are discussed in Section 4.4.

By overlaying the density field contours from Fig. 8a onto Fig. 7c, we can create a domain coloring with density contours as Fig. 8f. From Fig. 8f, it can be clearly seen that the change in density is gradual until just before the shock wave, which causes a sudden and significant shift in density. This results in dense contour lines, a considerable flow separation at the upper wall, and the shock wave branching off near both the upper and lower walls.

4.3 Density profiles

The streamwise density profiles at a constant height of $y/h^* = 0.5$ are shown in Fig. 9. The blue line represents an instantaneous density profile that corresponds to Fig. 8a. The red line indicates the time-averaged density profile calculated by

$$\bar{\rho} = \frac{1}{M}\sum_{i=0}^{M-1}\rho_i \tag{28}$$

where M is the number of data points used in the calculation. The black line depicts the curve calculated using one-dimensional isentropic theory. The error bars on the averaged density profile indicate the density standard deviation given by

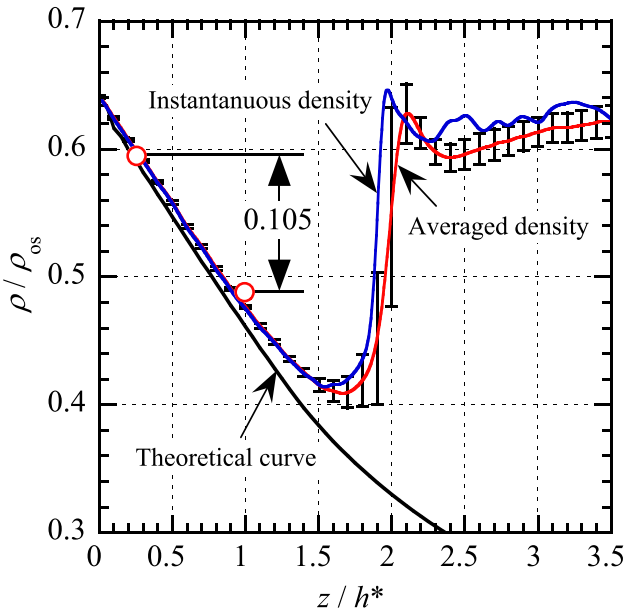

Fig. 9 Streamwise density profiles from the throat ($z/h^* = 0$) for $y/h^* = 0.5$. The background fringe is set to $\theta = 45°$. The blue and red lines are instantaneous and time-averaged density profiles, respectively, and the black line denotes the analytical curve calculated based on one-dimensional isentropic theory. Error bars relative to the time-averaged density profile indicate the standard deviation of the density fluctuations. The two white circles correspond to the two white circles in Fig. 5b

$$\sigma_\rho = \sqrt{\frac{\sum_{i=0}^{M-1}\left(\rho_i - \bar{\rho}\right)^2}{M}} \tag{29}$$

The theoretical density ratio at the duct throat ($z/h^* = 0$) is equal to $\rho^*/\rho_{os} = 0.634$.

Note that the two white circles in Fig. 9 correspond to those in Fig. 5b. The density at the location of the first white circle is determined using the theoretical value shown in Fig. 9, while the density at the location of the second white circle is calculated using Eq. (25). The density predicted by Eq. (25) aligns closely with the density measured using finite-fringe Mach-Zehnder interferometry. The white circles are approximately located at the center of the dark fringe patterns in Fig. 5b, corresponding to z/h^* values of about 0.25 and 1.0. Based on this, the spatial resolution in the z direction can be estimated as (1.0 − 0.25)×6 mm = 4.5 mm, which is approximately 150 times lower than the 31 μm resolution achieved by the finite-fringe interferogram.

We highlight here the fundamental difference in spatial resolution between the density fields reconstructed using the finite-fringe method and those obtained via the infinite-fringe method. In the finite-fringe approach, spatial resolution is governed by the pixel pitch of the digital image

sensor and the focal length of the imaging lens, because density values are assigned on a per-pixel basis, the resolution remains isotropic and invariant with respect to the viewing direction. Conversely, in the infinite-fringe method, spatial resolution is dictated by the spacing between adjacent interference fringes in the recorded interferogram. This spacing is inherently anisotropic, as the fringe distribution is typically non-uniform and varies with the observation angle. Such directional dependence must be carefully considered when interpreting the reconstructed density fields, particularly in applications requiring high spatial fidelity. It should be noted that the pseudo-infinite-fringe image shown in Fig. 7c is analytically reconstructed from Eq. 16. Accordingly, the spatial resolution is uniformly 31 μm, regardless of location or direction, since it inherits the resolution characteristics of the finite-fringe method.

The instantaneous and time-averaged densities decrease with increasing distance in the flow direction from the throat position to $z/h^* =$ about 1.7 just before a shock, almost like an isentropic curve. The difference between the experimental and theoretical values increases with increasing distance from the throat due to the viscous effect of the wall boundary layer. The shock wave oscillates back and forth in the flow direction (Ota et al. 2016; Yagi et al. 2017), resulting in a time-averaged density distribution that exhibits a slightly gentler density gradient and a marginally smaller increase in density compared to the instantaneous density distribution. Both distributions show a decrease in density immediately after the shock wave due to the effects of flow separation, followed by a gradual increase in density downstream. The freestream Mach number immediately before the shock can be estimated from the minimum of the time-averaged density distribution, assuming isentropic flow, to be $M_1 = 1.47$. Assuming that the density ρ_2 immediately after the shock is a normal shock for $M_1 = 1.47$, the theoretical density ratio ρ_2/ρ_{os} is calculated (Liepmann and Roshko 2001) as

$$\frac{\rho_2}{\rho_{os}} = \frac{\rho_1}{\rho_{os}}\frac{\rho_2}{\rho_1} = \frac{2^{\frac{1}{\gamma-1}}(\gamma+1)M_1^2}{\left[(\gamma-1)M_1^2+2\right]^{\frac{\gamma}{\gamma-1}}} = 0.74 \tag{30}$$

with a specific heat ratio of $\gamma = 1.4$. The theoretical value is about 20% higher than the experimental value. Possible reasons for this significant difference between the experimental and theoretical values are that the shock surface is slightly tilted, not perpendicular to the flow, the effect of shock oscillation, and the fact that the shock interferes with the boundary layer to become a series of compression waves.

The flow upstream of the shock is supersonic and exhibits minimal oscillations. The magnitude of the error bars in the density profile significantly affects the Mach waves generated at the throat. These error bars can approximate the experimental uncertainty, suggesting that the density uncertainty in this experiment is about 2.0% for atmospheric density. The uncertainties related to the experimental density are discussed in Section 4.5.

4.4 Shock oscillations

Ota et al. (2016) investigated the behavior of an oscillating shock in a transonic diffuser using high-speed Mach-Zehnder interferometry and high-speed laser schlieren techniques. The shock Mach number, or the incoming flow Mach number just upstream of the shock, is 1.1; hence, it is a typical normal shock. They also measured wall static pressures beneath the oscillating normal shock. The dominant frequency of the normal shock oscillation, measured with the high-speed Mach-Zehnder interferometer, showed good quantitative agreement with the frequency obtained from the high-speed laser schlieren. However, the frequencies of the normal shock oscillation derived from the wall pressure measurements were significantly lower than those obtained from both the high-speed laser schlieren and the high-speed Mach-Zehnder interferometry. In this study, the oscillatory characteristics of an unsteady shock with an incoming flow Mach number of 1.47, where the shock is strong enough to separate the boundary layer, are investigated quantitatively via the Lagrangian and Eulerian methods.

A shock motion can be examined from the bright-field schlieren shown in Fig. 8b, because of the large density gradient at the shock location. In this study, a threshold of a specific magnitude is established, and the shock motion is traced by identifying instances where the intensity exceeded this threshold as a shock. Figure 10a displays the shock motion at a height of $y/h^* = 0.5$ in Fig. 8b. The solid red line parallel to the vertical axis in Fig. 10a represents the time-averaged position of the shock motion. The dashed red lines represent the left and right limits, which are defined as the time-averaged shock position ($z/h^* = 1.97$) minus and plus twice the standard deviation of the shock oscillation, respectively. If the shock motion follows a Gaussian distribution, the shock position falls within its limits with a 95% probability. Note that according to Chauvenet's criterion, the shock will be within its limits with 75% probability regardless of the distribution it follows (Coleman et al. 2018). The time evolution of the density fluctuations at the time-averaged shock position ($z/h^* = 1.97$) for $y/h^* = 0.5$ is shown in Fig. 10b. The solid red line parallel to the horizontal axis shows the time-averaged density. Note that the time-averaged density in Fig. 10b matches the density value at the location of the steepest slope in the time-averaged streamwise density profile (Matsuo et al. 1993).

The oscillatory phenomena of shock waves are often discussed using skewness (Sk) and kurtosis (Ku) (Verma et al. 2018), defined, respectively, as

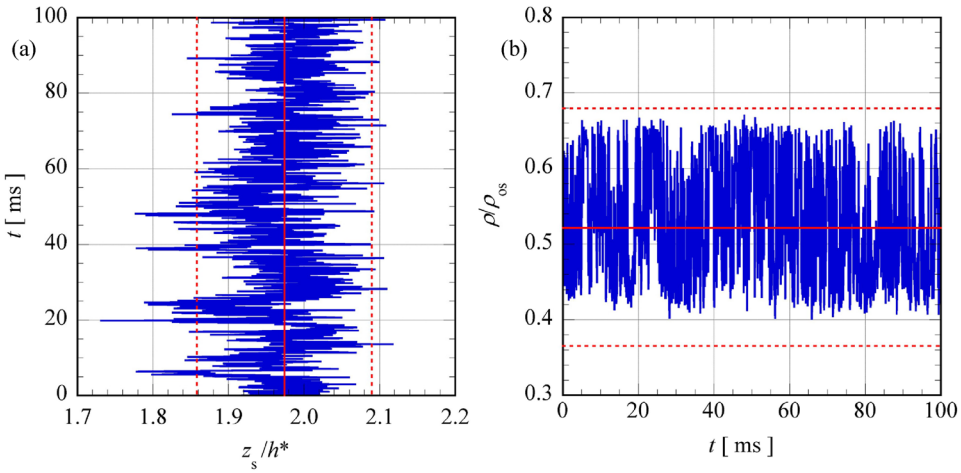

Fig. 10 Time histories for **a** shock oscillations and **b** density fluctuations where the experiment was performed at the background fringe pattern of $\theta = 45°$. The solid red line and dashed red lines in each graph denote the time-averaged quantity and the range of plus or minus two standard deviations, respectively

$$Sk_q = \frac{\sum_{n=1}^{N} \left(q_n - \bar{q}\right)^3}{N\sigma_q^3} \tag{31}$$

and

$$Ku_q = \frac{\sum_{n=1}^{N} \left(q_n - \bar{q}\right)^4}{N\sigma_q^4} - 3 \tag{32}$$

with $\bar{q} = \sum_{n=1}^{N} q_n/N$ where N is the number of data points, q represents a physical quantity, and σ_q is the standard deviation of q.

In statistical analysis, Sk and Ku are pivotal in characterizing the shape and symmetry of a distribution. Sk fundamentally contributes to the asymmetry of a distribution. When Sk approaches zero, the distribution exhibits symmetry around its mean. For a unimodal distribution (a distribution with a single peak), a positive Sk value signifies a right-skewed distribution (or distribution biased to the left), characterized by a long right tail, whereas a negative Sk value indicates a left-skewed distribution (or distribution biased to the right) with a long left tail. The magnitude of skewness is directly proportional to the absolute value of Sk. On the other hand, Ku quantifies the concentration of data around the mean. A high positive Ku value denotes a distribution with a pronounced peak and a greater concentration of data near the mean, surpassing the characteristics of a Gaussian distribution. In contrast, a negative Ku value reflects a flatter distribution with a diminished peak and extended tails. Typically, the majority of data points reside within two standard deviations of the mean ($\bar{q} \pm 2\sigma_q$). It is crucial to note that both Sk and Ku are zero for a Gaussian distribution. However, this condition alone does not suffice to confirm the Gaussian nature of the data. Specifically, while zero values of Sk and Ku are necessary for a distribution to be Gaussian, they are not sufficient conditions.

For the shock motion in Fig. 10a, $Sk_s = -0.313$ and $Ku_s = 0.145$. Consequently, it can be anticipated that the shock motion follows a Gaussian distribution. On the other hand, for density fluctuations in Fig. 10b, $Sk_s = 0.27$ and $Ku_s = -1.31$. Therefore, while the distribution of density fluctuations is nearly symmetric around the mean, it can be anticipated that "if there is a single peak", its value will be smaller and the width of the fluctuations broader compared to a Gaussian distribution.

A more detailed discussion of shock oscillations and density fluctuations can be made using a probability density function, pdf, defined as

$$pdf\left(q^\dagger\right) = \lim_{\Delta q^\dagger \to 0} \frac{\text{Prob}\left[q^\dagger < q^\dagger(t) < q^\dagger + \Delta q^\dagger\right]}{\Delta q^\dagger} \approx \frac{m}{N\Delta q^\dagger} \tag{33}$$

in the normalized form where $q^\dagger = (q - \bar{q})/\sigma_q$, $\Delta q^\dagger = 0.1$, m is the number of data in $\Delta q^\dagger$, and N is the number of data points. The area between the probability density function and the horizontal axis is 1.

The probability density functions for shock oscillations and density fluctuations are shown in Fig. 11 with red and blue circles, respectively. The solid red line denotes an approximate curve for the red circles, and the solid black line is the Gaussian distribution, given by

$$pdf(q^\dagger) = \frac{1}{\sqrt{2\pi}} \exp\left(-q^{\dagger 2}\right) \tag{34}$$

Here, pdf means the probability that the value of physical quantities that change with time, such as shock position (z_s) and density (ρ), is within a certain quantity range ($\Delta q^\dagger$) at a certain time.

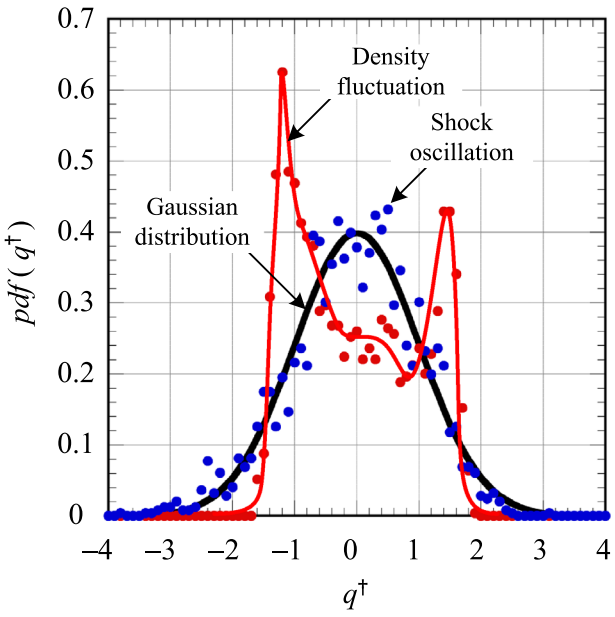

Fig. 11 Probability density functions for the shock oscillation (solid red line with red circles) and density fluctuation (blue circles) with Gaussian distribution (solid black line)

Figure 11 shows that shock oscillations follow a nearly Gaussian distribution except in the vicinity of $q^\dagger = 0$, but density fluctuations are distributed with large peaks on each side of $q^\dagger = 0$. For the two peaks of the probability density function of density fluctuations, the peak value at the negative $q^\dagger$ is higher than that at the positive $q^\dagger$. Experimental results similar to those of the present study were obtained in the past by Dolling et al. (1985), who investigated the unsteadiness of shock structure in attached and separated compression ramp flows using wall static pressure measurements. They showed that the probability density distribution for the pressure fluctuations is bimodal at the location where the pressure fluctuation is maximum.

The frequency response of shock oscillations and density fluctuations can be evaluated using the power spectrum. The power spectral density $G(f)$ of the fluctuation $q(t) - \bar{q}$ from the mean value $\bar{q}$ of a quantity $q(t)$ can be derived from its Fourier transform $Q(k)$ with the conjugate $Q(k)^*$ as follows:

$$G(f) = \frac{TQ(k) \cdot Q^*(k)}{N^2} \tag{35}$$

where T (approximately 200 ms) represents the total duration of the measurement, N (5, 000) denotes the number of data points, k ranges from 0 to $N/2 - 1$, f is defined as $k\Delta f = k/(N\Delta t)$, and $Q(k)$ is the discrete Fourier transform of $q(t) - \bar{q}$, given by

$$Q(k) = \sum_{n=0}^{N-1} (q(n\Delta t) - \bar{q}) \exp\left[-i\frac{2\pi kn}{N}\right]$$

The power spectral densities, G_s and G_ρ, corresponding to the shock motions and density fluctuations, respectively, are depicted in Fig 12a and b. The results are plotted in the form fG/σ^2 on linear-log axes. In this form, the area under a given curve segment is linearly proportional to the contribution of that particular frequency range to the overall signal variance σ^2 (Dolling and Smith 1989). Numerous previous experiments have been conducted to investigate the unsteady characteristics of an oscillating shock by installing pressure sensors beneath the shock foot. However, it is challenging to predict the time-averaged shock position in advance, which often results in the sensor locations not aligning with this average position. This limitation is an inherent drawback of using pressure sensors to capture the spectral distribution of shock motion, as they cannot be deployed with high spatial resolution. In contrast, the present experiment utilizes a very high spatial resolution for density measurements. As a result, the power spectral density profiles obtained from both

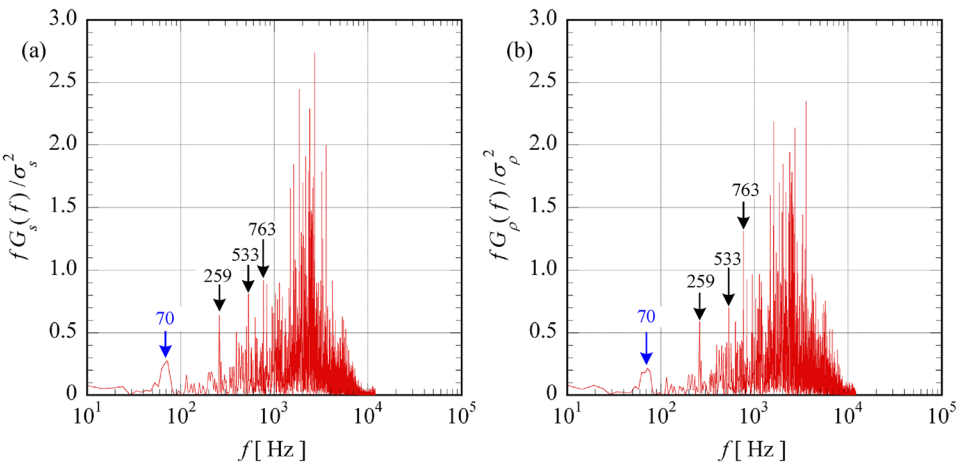

Fig. 12 Power spectral densities for **a** shock oscillations and **b** density fluctuations, which correspond to Fig. 10a and b, respectively

Lagrangian and Eulerian methods are found to be nearly identical. For instance, the 70 Hz spectrum indicated by the blue downward arrow, and the three spectra at 259 Hz, 533 Hz, and 763 Hz indicated by the black downward arrows, are clearly observable in both distributions. Unlike the blue spectrum, the black spectra are approximately harmonics of the lowest spectrum, suggesting they represent different physical phenomena. In the near future, these phenomena will be investigated in detail using data-driven analyses (Brunton and Kutz 2022) such as proper orthogonal decomposition (POD), dynamic mode decomposition (DMD), and spectral POD, along with three-dimensional large eddy simulations. These approaches are central to the methodological contributions of this study, which aims to establish a robust and generalizable strategy for analyzing complex flow structures in supersonic regimes.

Although the power spectra of the shock motion and density fluctuation exhibit similar distributions, their probability density functions appear distinct at first glance. However, upon closer examination of the probability density function for shock motion, it seems to exhibit peaks on either side of the mean.

4.5 Uncertainty analysis

Our first step is the evaluation of bias errors using Eq. (22). Considering that the spanwise duct width L has an error of less than 0.01%, the Gladstone-Dale constant K varies slightly with wavelength, but to a very small degree (Liepmann and Roshko 2001), and the wavelength error is of two orders of magnitude smaller compared to the phase error Telega et al. (2022), the derivative of Eq. (22) gives

$$d\rho = \frac{\lambda_0}{2\pi KL} d\tilde{\varphi} \tag{36}$$

In the present experiment, the spatial resolution for obtaining density fields is $\Delta s = 31\ \mu$m and the fringe interval is $b = 263\ \mu$m. Assuming 10% of the spatial resolution as the fringe shift error, a rough estimate of the phase error gives $B_{\tilde{\varphi}} = 2\pi\Delta s \times 0.1/b = 0.074$ rad. This value is approximately half of the estimate (0.13 rad) by Houwing et al. (2005). Given the above discussion, the bias error of the density is $B_\rho = 2.20 \times 10^{-3}$ kg/m^3 or 0.12 % to the stagnation density ρ_{os}.

To obtain an ensemble average density $\hat{\rho}$, experiments were conducted at background fringe directions of $\theta = 0°$, 45° , 90° , and 135°. Notably, the experiment at $\theta = 90°$ was performed twice, because the deformed fringes often collapsed in the vicinity of the shock, causing significant errors in the phase-unwrapping. Subsequently, the precision error S_ρ of the sample of n measurements was calculated by

$$S_\rho = \sqrt{\frac{\sum_{i=1}^{n} \left(\rho_i - \hat{\rho}\right)^2}{n(n-1)}} \tag{37}$$

with $\hat{\rho} = \sum_{i=1}^{n} \rho_i / n$.

The uncertainty error U_ρ for the 95% confidence interval is defined as follows (Coleman et al. 2018):

$$U_\rho = \sqrt{B_\rho^2 + (t_{95} S_\rho)^2} \tag{38}$$

where t_{95} can be obtained from the student's t-distribution as $t_{95} = 2.78$ for $n = 5$.

The time-averaged streamwise density distributions at a constant height of $y/h^* = 0.5$ are shown in Fig. 13 as solid blue line ($\theta = 0°$), solid red line($\theta = 45°$), solid ocher line($\theta = 90°$), and dashed red line($\theta = 135°$). As indicated by the solid blue lines, two experimental results are depicted for $\theta = 90°$. In addition, the density uncertainty in the normalized form (U_ρ/ρ_{os}), obtained from Eqs. (37) and (38), is illustrated by the light blue solid lines. Furthermore, the standard deviation of the density variation in the normalized form (σ_ρ/ρ_{os}), calculated using Eq. (29) for an angle of $\theta = 45°$, is represented by the solid green line in Fig. 13.

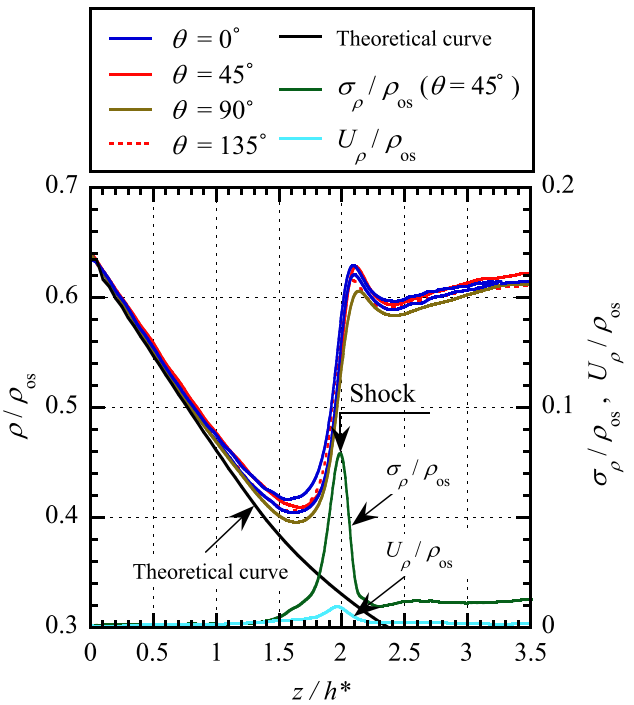

Fig. 13 Effects of shock oscillations on uncertainty. σ_ρ and U_ρ denote the standard deviation of shock oscillation from the experiment for the background fringe pattern of $\theta = 45°$ and the uncertainty for time-averaged streamwise density distributions for $y/h^* = 0.5$. The black line denotes the analytical curve calculated based on one-dimensional isentropic theory

For $\theta = 0°$, there were many cases where the interference fringes were collapsed in the vicinity of the shock and no phase unwrapping could be made during density reconstruction. On the contrary, the density reconstruction for $\theta = 45°$ and 135° was found to be easy and reproducible. Good quantitative agreement is reached between the density profiles of $\theta = 45°$ and 135°. Hence, we recommend that the direction of the wavefront of the background fringe pattern should be oblique to the direction of the shock wavefront.

Matsuo et al. (Matsuo et al. 1993) demonstrated experimentally that the peak values in the root mean square profile of static pressure oscillations along the duct axis correspond to the time-averaged locations of the shocks in a pseudo-shock. A closer examination of Fig. 13 reveals that the peak location in the standard deviation profile corresponds closely to the position of the maximum density gradient in the time-averaged density profile, i.e., the location where the shock is generated. A comparison between Figs. 10a and 13 shows that the shock position averaged in time aligns with the highest positions of uncertainty and the standard deviation of density fluctuations.

Next, we examine how shock oscillations affect the uncertainty in measuring density. The regions to be verified are divided into three categories: (i) upstream of the shock ($z/h^* = 0$ to 1.5), (ii) the region where shock oscillation is dominant ($z/h^* = 1.5$ to 2.5), and (iii) downstream of the shock ($2.5 < z/h^*$). In region (i), the uncertainty ($U_\rho/\rho_{os} = 0.11$ %) is comparable to the standard deviation ($\sigma_\rho/\rho_{os} = 0.14$ %). In region (ii), the peak uncertainty ($U_\rho/\rho_{os} = 0.95$ %) is about one-eighth of the peak standard deviation ($\sigma_\rho/\rho_{os} =$ 7.9 %). In region (iii), the uncertainty ($U_\rho/\rho_{os} = 0.19$ %) is about one-sixth of the standard deviation ($\sigma_\rho/\rho_{os} = 1.2$ %).

5 Concluding remarks

The methodology for extracting the time-resolved density field over the entire viewing area using Mach-Zehnder interferometry (MZI) with the finite-fringe setting is described in detail, such as the generation of background fringe patterns, the extraction of phase information, and the reconstruction of the density field. Applying these steps to transient flows with an oscillating shock in a divergent duct, where the shock has an incoming flow Mach number of 1.47 with bifurcation toward the upper and lower walls, was provided.

Finite-fringe interferograms of time-resolved density fields with the oscillating shock were taken using the MZI where the wavefront of the background interference fringe was oriented at $\theta = 0°$, 45°, 90°, and 135° to the horizontal plane. The fringe shift analysis was performed via a two-dimensional Fourier transform technique. An infinite-fringe interferogram of the same density field was also taken for comparison. The infinite-fringe interferogram is useful for identifying features such as shock locations and geometries, and the extent of boundary-layer separation. However, the spatial resolution for the density field is very poor compared to that obtained from the finite-fringe MZI. In the present experiment, the spatial resolution of the finite-fringe mode is 31 μm, which is approximately 150 times higher than the 4.5 mm resolution of the infinite-fringe mode along a fixed height of $y/h^* = 0.5$ upstream of the shock wave. At $\theta = 90°$, the deformed fringes may collapse in the vicinity of the shock, causing significant errors in the phase unwrapping. The reconstructed density fields for $\theta = 5°$ and 10° agree quantitatively. Hence, it is recommended that the direction of the wavefront for the background fringe pattern be tilted rather than aligned parallel to the shock wavefront.

In addition to the density contour map, several innovative flow visualizations were presented, including bright-field schlieren imaging, pseudo-infinite-fringe interferograms, and domain coloring. While finite-fringe interferograms do not reveal the details of the shock structure, it is possible to easily generate infinite-fringe interferograms from the finite-fringe ones to observe those details. The domain coloring incorporates phase information along with the density field, resulting in a vivid color representation of the shock structure.

The oscillatory characteristics of shock motions are examined using both Lagrangian and Eulerian methods. The former method focuses on the time evolution of the shock position, as captured by bright-field schlieren imaging, while the latter method analyzes the time history of the density at the time-averaged shock position determined by the Lagrangian approach. In addition, the shock behavior obtained by both methods was evaluated by probability density functions and power spectral density functions. It was observed that the probability density function of shock motions adheres to a nearly Gaussian profile, except in the vicinity of the time-averaged location. Conversely, the probability density distribution of density fluctuations exhibits a bimodal pattern. The spectral characteristics obtained from both approaches show almost quantitative agreement.

An uncertainty analysis of density measurements via MZI with the finite-fringe setting was conducted, revealing that phase-shift errors are the primary source of bias errors. The density uncertainty was assessed in three regions: (i) the supersonic area upstream of the shock, (ii) the shock oscillation area, and (iii) the subsonic region downstream of the shock. It can be seen that in areas (ii) and (iii), where shock oscillations have an effect, the density uncertainty is negligibly small compared to the magnitude of the density fluctuations. The uncertainty in density and the mean square of density fluctuations due to shock oscillation were found to peak at the time-averaged shock location.

To the best of the authors' knowledge, no previous studies have reported time-resolved, high-spatial-resolution

measurements of two-dimensional density fields—including oscillating shock waves—within the same measurement section as employed in the present study. As such, a direct comparison between the present method and existing diagnostic techniques is not currently feasible. Instead, the standard deviation and uncertainty of density fluctuations were experimentally quantified in the region of shock wave oscillation and its surrounding areas. These results are expected to serve as benchmark data for future validation and comparison of alternative measurement approaches.

Future work will involve experiments conducted under identical flow conditions using a rainbow schlieren optical system and a Twyman–Green interferometer, both available in our laboratory, to assess the influence of different diagnostic techniques on time-resolved density field measurements. In addition, comparisons with ongoing large eddy simulations are planned to further evaluate the accuracy and applicability of the present method.

Appendix: Procedure for density field reconstruction

The workflow for reconstructing time-resolved two-dimensional density fields from RGB interferogram sequences is summarized in the flowchart below:

Step 1: Grayscale Conversion

The original RGB interferogram images are converted into 8-bit grayscale representations to simplify intensity analysis and reduce computational complexity. In this step, Fig. 4a and b is transformed into grayscale datasets to facilitate subsequent quantitative evaluation.

Step 2: Region of Interest (ROI) Extraction

A rectangular mask, denoted as rect(x, y), is applied to crop the image and isolate the region containing meaningful fringe patterns, thereby excluding irrelevant peripheral areas.

Step 3: Fourier Transform

A two-dimensional (2D) Fourier transform is performed on the cropped grayscale image to transition from the spatial domain to the frequency domain, with the DC component centered. Figure 6a and b is generated through this transformation, and the resulting data are visualized in grayscale.

Step 4: Spectral Peak Identification

In the frequency domain, three distinct spectral peaks are identified: one at the origin and two symmetrically located on either side, corresponding to the carrier frequencies of the fringe pattern. These peaks are denoted as G_0, G_1, and G_1^*, respectively, and are clearly visible in Fig. 6a and b.

Step 5: Carrier Spectrum Selection and Coordinate Shifting

One of the symmetric carrier spectra, typically G_1, is selected and shifted to the origin of the frequency domain via a coordinate transformation. This facilitates accurate phase extraction by centering the modulated carrier information.

Step 6: Bandpass Filtering

A rectangular bandpass filter is applied to isolate the selected carrier spectrum by removing all other spectral components. At this stage, only the G_1 component is retained, ensuring that the modulated fringe information is preserved.

Step 7: Inverse Fourier Transform

An inverse 2D Fourier transform is applied to the filtered spectrum to reconstruct the complex fringe-modulated image in the spatial domain. This operation yields a complex-valued representation of the fringe pattern associated with c_t.

Step 8: Phase Extraction via Logarithmic Transformation

The natural logarithm of the reconstructed complex image is computed to separate amplitude and phase components, enabling extraction of the wrapped phase distribution. This procedure corresponds to Eq. (20) and provides two-dimensional phase information at a specific temporal instance.

Step 9: Phase Unwrapping

The wrapped phase map is converted into a continuous phase distribution using the phase-unwrapping algorithm proposed by Herráez et al. (2002), making it suitable for quantitative analysis.

Step 10: Noise Reduction

The Block-Matching and 3D (BM3D) algorithm is employed to suppress noise in the unwrapped phase image while preserving fine structural details, thereby enhancing the fidelity of the reconstructed phase data.

Step 11: Density Field Reconstruction

The denoised phase map is transformed into a two-dimensional density field using the Gladstone–Dale relation, which accounts for optical path differences and refractive index variations. This step corresponds to Eq. (23) and yields the density field at a specific point in time.

Author contributions SN and YM contributed to the conceptualization; TY contributed to the data curation, formal analysis, and visualization; TY, MO, and HK contributed to the investigation; TY contributed to the software; SN contributed to the resources and project administration; SN and YM contributed to the supervision; MO and HK contributed to the validation; and TY and YM wrote the main manuscript text. All authors reviewed the manuscript.

Funding This work was supported in part by a Grant-in-Aid for Scientific Research(C) (Grant No. 20K04272).

Data availability No datasets were generated or analyzed during the current study.

Declarations

Conflict of interest The authors report no Conflict of interest.

Ethics approval and consent to participate Not applicable.

Conflict of interest The authors declare no Conflict of interest.

References

Atkin CJ, Squire LC (1992) Study of the interaction of a normal shock wave with a turbulent boundary layer at Mach numbers between 1.30 and 1.55. Eur J Mech B/Fluids 11(1):93–118

Benitez EK, Ceruzzi A, Gragston M, Parziale NJ, Schmidt BE, Weisberger JM (2025) Focused laser differential interferometry: recent developments and applications for flow measurements, AIAA Paper, 2025-2017

Brunton SL, Kutz JN (2022) Data-driven science and engineering: machine learning, dynamical systems, and control. Cambridge University Press

Carroll BF, Dutton JC (1990) Characteristics of multiple shock wave/turbulent boundary-layer interactions in rectangular ducts. J Propul Power 6(2):186–193

Coleman HW, Steele WG (2018) Experimentation, validation, and uncertainty analysis for engineers. John Wiley & Sons

Dolling DS, Or CT (1985) Unsteadiness of the shock wave structure in attached and separated compression ramp flows. Exp Fluids 3(1):24–32

Dolling DS, Smith DR (1989) Separation shock dynamics in Mach 5 turbulent interactions induced by cylinders. AIAA J 27(12):1698–1706

Feng T, McGuirk JJ (2016) Measurements in the annular shear layer of high subsonic and under-expanded round jets. Exp Fluids 57(1):7

Herráez MA, Burton DR, Lalor MJ, Gdeisat MA (2002) Fast two-dimensional phase-unwrapping algorithm based on sorting by reliability following a noncontinuous path. Appl Opt 41(35):7437–7444

Houwing AFP, Takayama K, Jiang Z, Sun M, Yada K, Mitobe H (2005) Interferometric measurement of density in nonstationary shock wave reflection flow and comparison with CFD. Shock Waves 14(1):11–19

Lempert WR, Jiang N, Sethuram S, Samimy M (2002) Molecular tagging velocimetry measurements in supersonic microjets. AIAA J 40(6):1065–1070

Léon O, Donjat D, Olchewsky F, Desse J-M, Nicolas F, Champagnat F (2022) Three-dimensional density field of a screeching under-expanded jet in helical mode using multi-view digital holographic interferometry. J Fluid Mech 947:A36

Liepmann HW, Roshko A (2001) Elements of gasdynamics, Courier Corporation

Mäkinen Y, Azzari L, Foi A (2020) Collaborative filtering of correlated noise: exact transform-domain variance for improved shrinkage and patch matching. IEEE Trans Image Process 29:8339–8354

Marsh AW, Kramer AN, Maranto KN, Chen MY (2024) Imaging focused laser differential interferometry. Opt Lett 49(8):2109–2112

Matsuo K, Mochizuki H, Miyazato Y, Gohya M (1993) Oscillatory characteristics of a pseudo-shock wave in a rectangular straight duct. Prog Aerosp Sci 35(1):33–100

Matsuo K, Miyazato Y, Kim HD (1999) Shock train and pseudo-shock phenomena in internal gas flows. JSME Int J, Ser B 36(2):222–229

Merzkirch W (2012) Flow visualization. Academic Press Inc

Ota T, Nakao S, Ono D, Miyazato Y (2016) Optical measurements of shock wave oscillations in transonic diffusers by high-speed Mach-Zehnder interferometers, AIAA Paper, 2016-1764

Ota M, Hamada K, Kato H, Maeno K (2011) Computed-tomographic density measurement of supersonic flow field by colored-grid background oriented schlieren (CGBOS) technique. Meas Sci Technol 22(10):104011

Parziale NJ, Shepherd JE, Hornung HG (2013) Differential interferometric measurement of instability in a hypervelocity boundary layer. AIAA J 51(3):750–754

Parziale NJ, Smith MS, Marineau EC (2015) Krypton tagging velocimetry of an underexpanded jet. Appl Opt 54(16):5094–5101

Rathakrishnan E (2019) Applied gas dynamics. John Wiley & Sons

Sakurai T, Handa T, Koike S, Mii K, Nakano A (2015) Study on the particle traceability in transonic and supersonic flows using molecular tagging velocimetry. J Vis 18(3):511–520

Settles GS (2001) Schlieren and shadowgraph techniques: visualizing phenomena in transparent media. Springer Science & Business Media

Settles GS, Fulghum MR (2016) The focusing laser differential interferometer, an instrument for localized turbulence measurements in refractive flows. J Fluids Eng 138(10):101402

Settles GS, Hargather MJ (2017) A review of recent developments in schlieren and shadowgraph techniques. Meas Sci Technol 28(4):042001

Srulijes J, Seiler F, Runne K (2000) Flow visualisation and pressure measurements on spike-tipped bodies, AIAA Paper, 2000-2520

Smits AJ, Lim TT (2012) Flow visualization: techniques and examples. Imperial College Press

Sugawara S, Nakao S, Miyazato Y, Ishino Y, Miki K (2020) Three-dimensional reconstruction of a microjet with a Mach disk by Mach-Zehnder interferometers. J Fluid Mech 893:A25

Sugawara S, Nakao S, Miyazato Y, Ishino Y, Miki K (2021) Quantitative flow visualization of slightly underexpanded microjets by Mach-Zehnder interferometers. Flow Turbul Combust 106(3):971–992

Szumowski AP, Obermeier F, Meier GEA (1995) Oscillation modes of laval nozzle flow. Exp Fluids 18(3):145–152

Takeda M (2013) Fourier fringe analysis and its application to metrology of extreme physical phenomena: a review. Appl Opt 52(1):20–29

Takeshita T, Nakao S, Miyazato Y (2019) Application of Mach-Zehnder interferometers for isolator shock trains. ACC J 25(1):68–77

Takeshita T, Fukunaga R, Nakao S, Miyazato Y, Miki K (2023) Quantitative flow diagnostics of shock trains by rainbow schlieren deflectometry. Aeronaut J 127(1309):428–445

Telega J, Szwaba R, Śmiałek MA (2022) Compressible gas density measurement by means of Fourier analysis of interferograms. Measurement 189:110458

Toker GR (2017) Holographic interferometry: a Mach-Zehnder approach. CRC Press

Verma S, Chidambaranathan M, Hadjadj A (2018) Analysis of shock unsteadiness in a supersonic over-expanded planar nozzle. Eur J Mech-B/Fluids 68:55–65

Wang GT, Peng Y, Guildenbecher DR, Lynch KP, Sun W, Mazumdar YC (2022) Hybrid interferometric diagnostic for the refractive index measurement across nearly discrete shock waves. Opt Lett 47(16):4159–4162

Wegert E (2012) Visual complex functions: an introduction with phase portraits. Springer Science & Business Media

Winckler J (1948) The Mach interferometer applied to studying an axially symmetric supersonic air jet. Rev Sci Instrum 19(5):307–322

Yagi S, Inoue S, Nakao S, Ono D, Miyazato Y (2017) Optical measurements of shock waves in critical nozzles at low Reynolds numbers. J Flow Control Measure Vis 5(2):36–50

Yoo J, Mitchell D, Davidson DF, Hanson RK (2010) Planar laser-induced fluorescence imaging in shock tube flows. Exp Fluids 49(4):751–759

Yüceil KB (2017) A comparison of PIV and interferometric Rayleigh scattering measurements in the near field of underexpanded sonic jets. Aerosp Sci Technol 67:31–40